Predicting Fracture Propensity in Amorphous Alumina from Its Static Structure Using Machine Learning

Du, Tao; Liu, Han; Tang, Longwen; Sørensen, Søren Strandskov; Bauchy, Mathieu; Smedskjær, Morten Mattrup

Published in:
ACS Nano

DOI (link to publication from Publisher):
10.1021/acsnano.1c05619

Publication date:
2021

Document Version
Accepted author manuscript, peer reviewed version

Predicting Fracture Propensity in Amorphous Alumina from Its Static Structure Using Machine Learning

Tao Du[1], Han Liu[2], Longwen Tang[2], Søren S. Sørensen[1], Mathieu Bauchy[2,*], Morten M. Smedskjaer[1,*]

[1] *Department of Chemistry and Bioscience, Aalborg University, Aalborg 9220, Denmark*

[2] *Physics of AmoRphous and Inorganic Solids Laboratory (PARISlab), Department of Civil and Environmental Engineering, University of California, Los Angeles, CA 90095, USA*

* Corresponding authors. email: bauchy@ucla.edu (M.B.), mos@bio.aau.dk (M.M.S.)

Abstract

Thin films of amorphous alumina (a-Al_2O_3) have recently been found to deform permanently up to 100% elongation without fracture at room temperature. If the underlying ductile deformation mechanism can be understood at the nanoscale and exploited in bulk samples, it could help to facilitate the design of damage-tolerant glassy materials–the holy grail within glass science. Here, based on atomistic simulations and classification-based machine learning, we reveal that the propensity of a-Al_2O_3 to exhibit nanoscale ductility is encoded in its static (non-strained) structure. By considering the fracture response of a series of a-Al_2O_3 systems quenched under varying pressure, we demonstrate that the degree of nanoductility is correlated with the number of bond switching events, specifically the fraction of five- and six-fold coordinated Al atoms, which are able to decrease their coordination number under stress. In turn, we find that the tendency for bond switching can be predicted based on a non-intuitive structural descriptor calculated based on the static structure, namely, the recently developed "softness" metric as determined from machine learning. Importantly, the softness metric is here trained from the spontaneous dynamics of the system (*i.e.*, under zero strain) but, interestingly, is able to readily predict the fracture behavior of the glass (*i.e.*, under strain). That is, lower softness facilitates Al bond switching and the local accumulation of high-softness regions leads to rapid crack propagation. These results are helpful for designing glass formulations with improved resistance to fracture.

Keywords

amorphous oxides; molecular dynamics simulation; nanoductility; machine learning; fracture

Graphical abstract

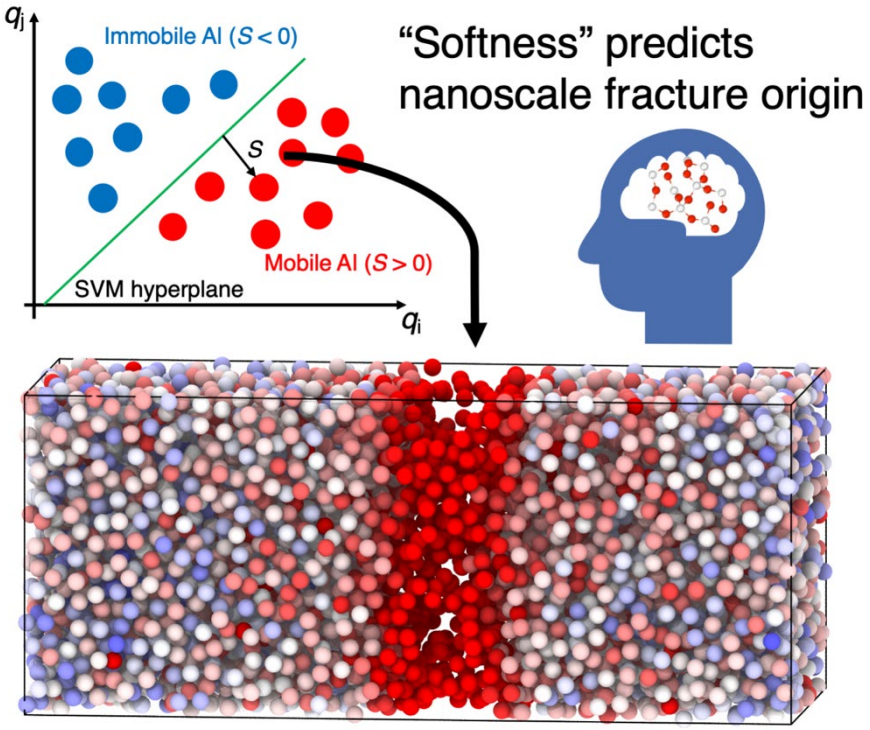

Oxide glasses find a range of applications, from window panels and touchscreen displays to optical fibers for internet communication and vaccine vials for fighting the COVID-19 pandemic. This is due to their desirable properties such as transparency, formability, thermal and chemical durability, as well as tailorable composition without stoichiometric requirements. However, oxide glasses are usually considered brittle, as they fracture catastrophically without plastic deformation at the macroscale, greatly hindering many applications.[1–3] It is therefore essential to gain a deeper understanding of the deformation and fracture mechanisms of this material family.[4]

In general, it is possible to induce brittle to ductile transitions in glasses and amorphous materials by tailoring their nanostructure through composition modification,[5–7] thermal treatments,[8,9] densification,[10] *etc*. In crystalline materials, fracture is affected by the competition between dislocations and bond breaking, with plasticity typically being initiated at defects.[5] However, the origin of ductility remains poorly understood in non-crystalline materials, since there are no well-defined defects in such materials due to the lack of long-range ordered structure. Even when the positions of all atoms in the static structure of a glass are fully known, it remains very challenging to identify the soft regions that are vulnerable to rearrangements.[11,12] Several models have been proposed to account for the plastic properties of glasses, including elastoplastic,[13] soft glassy rheology,[14] and shear transformation zone[15,16] models. In metallic glasses, ductility is found to be related to the rearrangements of local structure, known as shear transformation zones.[17] In contrast, the brittle nature of oxide glasses has been attributed to the lack of such regions of plastic deformation. Although these theories have proposed the existence of defects in the glass structure, they are unfortunately phenomenological and fail to provide a precise definition of these defects, thus hindering their identification from first principles.[18] Recently, several data-driven models have been proposed to forecast the propensity of particles or atoms to rearrange.[19–22] However, due to the structural complexity of amorphous materials, the correlations between the structure and fracture mechanism in oxide glasses remain unknown.

To predict the tendency for crack propagation in oxide glasses based on their initial structure, it is necessary to first understand the correlation between structure and local atomic dynamics. Some structural descriptors such as local density, free volume, or bond orientational order can be correlated with flow defects, but are insufficient for fully predicting glass fracture.[18] As a promising alternative path, advances within machine learning have made it possible to predict non-intuitive structural descriptors using algorithms such as support vector machine (SVM),[19] graph neural network,[23] and convolutional neural network.[20] Among these, the non-intuitive structural metric termed “softness” derived from SVM is found to be strongly correlated with the dynamics of specific atoms only based on their local structural environments. Note that although the order parameters used to construct the softness metric are simple two- or three-body order parameter terms, we refer to it as non-intuitive as it is calculated from the hyperplane constructed by the SVM classifier in the high dimensional space formed by all the order parameters. Generally, the atoms with higher softness are more susceptible to rearrange, or equivalently, to be regarded as flow defects. The softness descriptor has been successfully adopted in understanding the dynamical heterogeneities at the glass transition,[22] creep dynamics of gels,[21] yielding behavior of disordered solids,[24] dynamics of grain boundaries in polycrystals,[25] thin film glass dynamics,[26] and crystallization kinetics at the solid-liquid interface.[27] Here, inspired by this approach, we explore

whether the fracture behavior of amorphous oxides (which is governed by the local propensity of atoms to rearrange) is encoded in their static structure, and whether the spontaneous dynamics (driven by temperature) has sufficient information encoded to predict the stress-driven dynamics during fracture.

By isolating nanoscale features of the glass structure that control the dynamics and mechanics of the macroscopic material, the era of nano-engineering of glasses could be unlocked, as inspired by the Materials Genome Initiative[28] – in strong constrast to the traditional Edisonian trial-and-error approach for exploring composition-property relations. As an example, understanding the behavior of glasses at the nanoscale has been revealed to facilitate the fabrication of glasses with enhanced plastic deformation.[29,30] Two other prominent examples include the fracture behaviors of amorphous alumina (a-Al_2O_3) and glassy silica at the nanoscale, which have been intensively studied. For silica, a brittle-to-ductile transition can be achieved through pressure quenching,[10] reducing the sample size to the nanoscale,[31] consolidating glassy nanoparticles,[32] or exposure to an electron beam.[33] For a-Al_2O_3, depending on the loading conditions, some studies indicate plastic deformation at room temperature,[34–37] while others report a-Al_2O_3 to behave fully brittle.[38–40] Recently, pronounced plasticity in flaw-free thin films of a-Al_2O_3 at high strain rate has been attributed to a viscous creep mechanism, which is associated with Al bond switching events, *i.e.*, decreasing or increasing coordination number and swapping of oxygen neighbors.[37] Such bond switching generates localized strain events, which accumulate into macroscopic flow. It is proposed that the bond switching activity leading to mechanical relaxation is more likely to occur in nanoscale alumina than in silica, partly due to the more compact structure of a-Al_2O_3.[37] Although the nanoscale plasticity in a-Al_2O_3 has been ascribed to a viscous creep mechanism, the structural drivers for bond switching have not yet been revealed. This seriously limits our ability to exploit this mechanism of plasticity enhancement in bulk oxide glasses. That such exploitation at a larger scale is indeed possible has been highlighted in our recent study, where we reported a record-high fracture toughness (1.4 MPa $m^{0.5}$) in a bulk oxide glass with high propensity for bond switching.[41] As such, an improved understanding of deformation and fracture mechanisms of glasses at the nanoscale is needed to improve their mechanical performance at the macroscale.

In this study, we investigate the structural origin of the ductile deformation behavior observed in a-Al_2O_3. We do so in different pressure-quenched samples to vary the density, atomic structure, and thus propensity for bond switching.[37,41] To obtain atomic scale information about the fracture mechanism, we use molecular dynamics (MD) simulations to establish our conclusions since *in situ* mapping of atomic rearrangements during fracture are still out of reach experimentally. The densified a-Al_2O_3 samples are then subjected to uniaxial tension and the fracture response is compared with bond switching analyses as well as the softness metric determined using SVM. We show that the degree of nanoductility in densified a-Al_2O_3 is related to the decrease in the coordination number of five- and six-fold coordinated Al atoms, with the fraction of these units increasing with a decrease in the average softness of Al atoms. Specifically, lower softness facilitates Al bond switching and the local accumulation of high-softness regions leads to rapid crack propagation.

Results and discussion

Mechanical response of densified a-Al_2O_3

To obtain the datasets needed as input for machine learning, we first simulate the fracture behavior of densified a-Al_2O_3 samples under different loading conditions, since these conditions influence the simulated fracture response for a-Al_2O_3.[37] The stress-strain curves of a-Al_2O_3 under the first loading condition (plane stress) is shown in Fig. S1. Consistent with Ref. [37], we find that a-Al_2O_3 exhibits a fairly ductile response under this loading condition. The total strain can reach values up to 50% without fracture for all the pressures used to pre-densify a-Al_2O_3. However, this makes it difficult to identify the differences in the ability of the densified a-Al_2O_3 samples to undergo plastic deformation. Therefore, we apply the second loading condition (plane strain), as shown in the inset of Fig. 1A. The mechanical response is significantly influenced by the loading condition, with all the samples exhibiting a fairly brittle response, as manifested by a sudden drop in the stress-strain curve upon rapid crack propagation (see Fig. 1A). We note that after reaching the first maximum stress, all the a-Al_2O_3 samples exhibit nearly constant stress with an increase in the strain before failure (*i.e.*, yielding regime) due to the existence of plastic deformation. Importantly, with an increase in the pressure during quenching, the yielding regime becomes more pronounced, showing that the more densified a-Al_2O_3 samples feature improved nanoductility (see Fig. 1B). Atomic snapshots of the fracture evolutions of a-Al_2O_3 samples densified at 0 and 4 GPa are shown in Fig. S2. We note that densification-induced nanoductility has also been observed in amorphous silica.[10]

We then calculate the cumulative non-affine displacement (D) of each Al atom (see Methods section) to understand the carriers of plasticity during fracture under the second loading condition (plane strain). Since D represents the irreversible structural rearrangements of each atom, it has been successfully applied to identify the activation of STZs of various amorphous systems during fracture.[42] Figure 1C illustrates how the non-affine displacement captures the rearrangement of the particles by isolating the non-affine motion associated with local rearrangements from the best-fit affine deformation of its neighborhood. As shown in Fig. 1D, we observe that with an increase in pressure during quenching, the Al atoms tend to have larger values of D, indicating an increasing extent of structural reorganization during the fracture process. Since the non-affine displacement reflects the plasticity events of the atoms under stress,[42] densification of a-Al_2O_3 improves the nanoductility by facilitating non-affine reorganizations of the Al atoms. This is reflected through the linear growth of plastic energy with the cumulative non-affine displacement D of Al atoms as shown in Fig. S3.

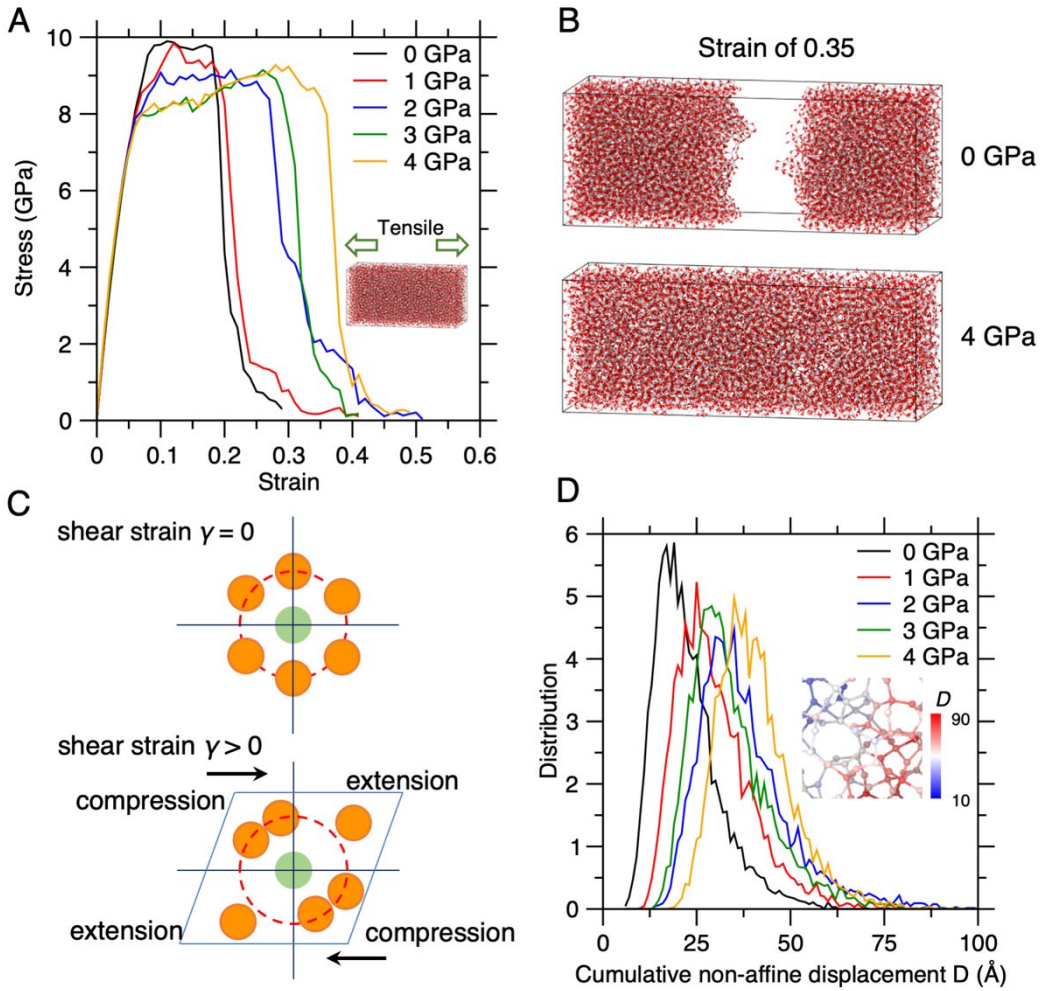

Fig. 1 (A) Stress-strain curves of densified a-Al_2O_3 under the second loading condition (plane strain); (B) Atomic snapshot of a-Al_2O_3 at $\varepsilon = 0.35$. Al and O atoms are represented by white and red spheres, respectively; (C) Schematic showing the non-affine displacement induced by applying a shear deformation γ. The non-affine displacement of the central atom in green at strain γ is captured by the best-fit affine transformation of the neighboring atoms with reference to the initial configuration; (D) Distribution of the cumulative non-affine displacement D of the Al atoms during the tensile process for the different densified a-Al_2O_3 samples.

Stress-induced bond switching events

In the following, we analyze the bond switching activities as a function of strain to correlate the non-affine reorganizations with the bonding state of Al atoms. The bond switching activities are defined as the changes in the coordination environment of Al atom, *i.e.*, whether the coordination number (CN) decreases or increases or if a neighbor oxygen is swapped by another one compared to the non-strained configuration. As shown in Figs. 2A-C, the extent of all three bond switching events increases with an increase in strain. This indicates that structural reorganizations can be achieved though bond switching, which dissipates the strain energy during fracture.[41] When comparing the extent of bond switching events under the two different loading conditions, we find the main difference to be the fraction of swapped CN at the final strain of 0.5 (see results for the first and second loading condition in Fig. S4C and Fig. 2C, respectively). That is, the final swapped CN fraction is in the range of 40-55% and 20-35% for first and second loading condition, respectively. We also observe that the pressure dependence of the swapped CN fraction in the two

loading conditions is inverse, indicating that the swapped CN is related to the loading conditions. This is due to the fact that all the bond switching events facilitate nanoductility by allowing the structure to reorganize instead of allowing crack propagation. For the first loading condition (plane stress), all samples exhibit the same nanoductility by having almost the same number of bond switching events (around 90% when considering all the bond switching events). When the sample is quenched at a higher pressure, the over-coordinated Al atoms are more prone to decrease their CN upon deformation. Consequently, samples quenched at high pressures have a lower fraction of the swapped CN events under the first loading condition.

Since the fraction of decreased CN is enhanced by densification for both loading conditions (see Figs. 2A and S4A), we infer that the pressure-induced plasticity can be associated with the activities related to decreased CN. The accumulated rise in the decreased CN activities in the densified a-Al_2O_3 implies that more potential energy has been dissipated through the breakage of Al-O bonds, which allows for less stress accumulation in the glass during tensile loading and thus improves nanoductility. In the remaining part of this paper, we will focus on understanding the structural origin of the densification-induced nanoductility in a-Al_2O_3 for the second loading condition (plane strain), for which the largest differences in fracture response are observed. The atomic snapshots of Al atoms undergoing three bond switching activities at $\varepsilon = 0.2$ are shown in Fig. 2D. For the a-Al_2O_3 sample quenched at 0 GPa, we observe that a crack has already propagated at $\varepsilon = 0.2$. By analyzing the bond switching activities, we find that Al atoms undergoing decreased CN and swapped CN are mainly located in the vicinity of the crack, highlighting the spatial distribution of bond switching activities.

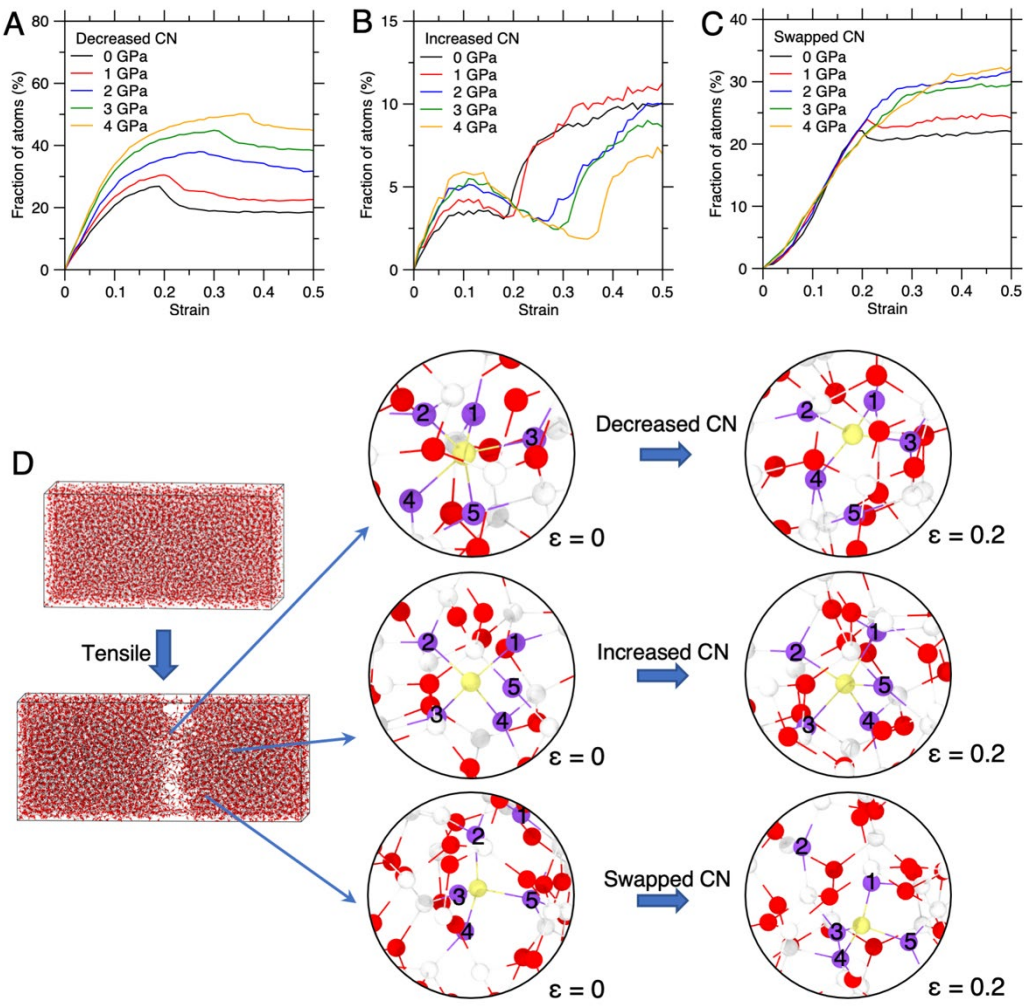

Fig. 2 Fraction of Al atoms subjected to the bond switching activities under the second loading condition. (A) Decreased CN, (B) Increased CN, and (C) Swapped CN relative to the coordination environment in the non-strained configuration. (D) Atomic snapshots of bond switching activities in a-Al_2O_3 of 0 GPa upon tension. Top: Example of a decreased CN of Al (in yellow): The CN of Al is five at ε = 0, and decreases to four at ε = 0.2. Middle: Example of an increased CN of Al (in yellow): The CN of Al increases from four to five when ε increases from 0 to 0.2. Bottom: Example of a swapped CN of Al (in yellow) first connected to four O atoms (number 2, 3, 4 and 5) at ε = 0, but as ε increases to 0.2, the CN of Al remains four while connecting to a new O atom number 1.

The initial configurations of the a-Al_2O_3 samples are affected by the applied pressure, which in turn impacts the fracture response. To investigate this, we first compute the CN of Al atoms of the non-strained structure, and classify them into decreased CN, increased CN, and swapped CN based on the bond switching activities at a strain of 50%. We first observe that the CN states of Al atoms are significantly influenced by the applied pressure. The fractions of 5-fold Al atoms (Al^5) and 6-fold Al atoms (Al^6) increase at the expense of 4-fold Al atoms (Al^4) with an increase in the quenching pressure (Fig. S5). Notably, we observe that the initial state of Al atoms significantly influences the bond switching activities during fracture. Specifically, Al^6 species exhibit the largest degree of decreased CN, while Al^4 species exhibit the largest degree of increased or swapped CN upon fracture (Fig. 3A). This can be understood from the fact that Al^6 units are formed due to the application of pressure during cooling, but remain stuck in their overcoordinated state during the

final zero pressure relaxation. At this point, these over-coordinated units are in a metastable equilibrium state. The following application of a tensile stress then allows them to quickly relax toward the more stable 5- or 4-fold coordinated states while dissipating energy within the structure. Based on the bond switching results under two loading conditions (Figs. 2A and S4), the pressure-induced nanoductility is mainly attributed to the decreased CN of Al^5 and Al^6 atoms, as the fractions of Al^6 and Al^5 species that decrease their CN increase with increasing pressure (Fig. 3A).

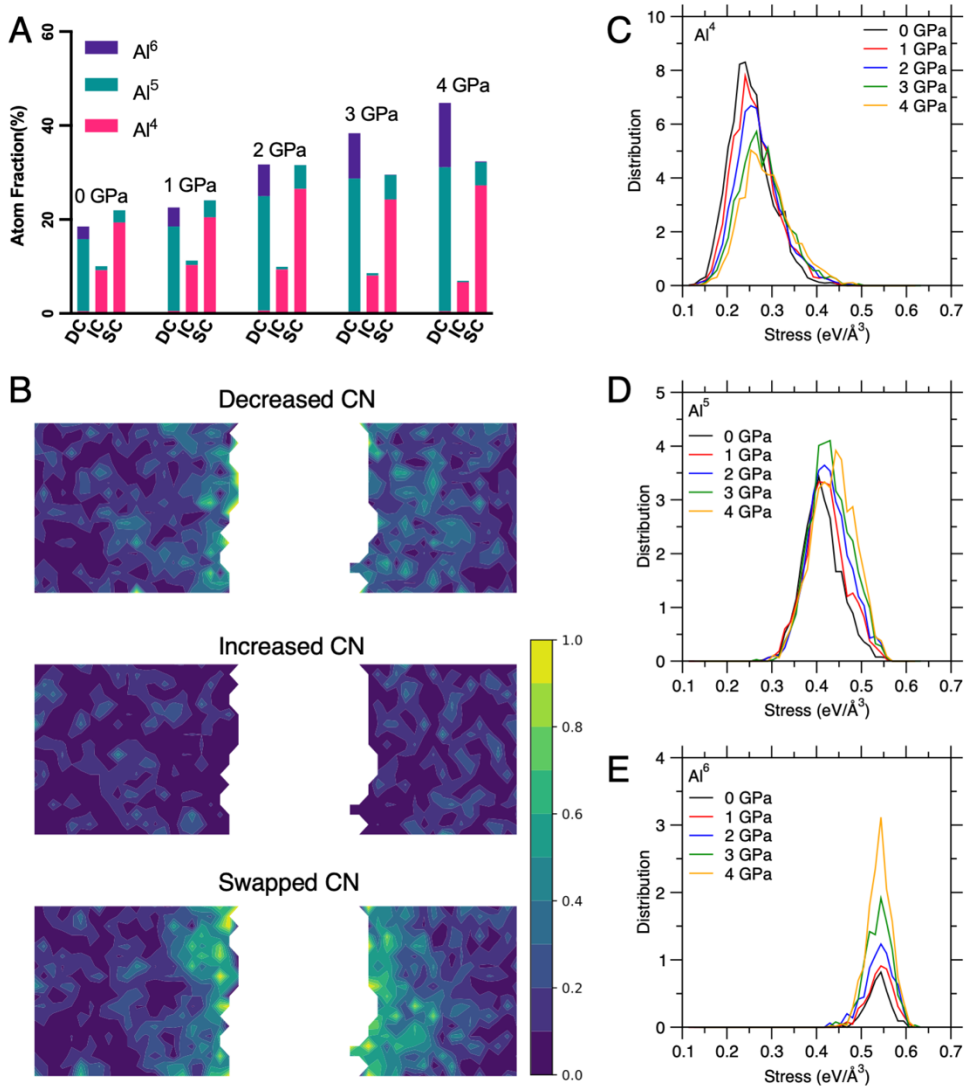

Fig. 3 (A) Fractions of different Al species subjected to bond switching activities upon fracture in the five different densified samples. Here, DC, IC, and SC represent decreased CN, increased CN, and swapped CN, respectively. (B) Spatial distribution of the normalized fraction of Al atoms with decreased CN, increased CN, and swapped CN. The calculations are based on a-Al_2O_3 formed under 0 GPa at $\varepsilon = 0.5$. (C,D,E) Distribution of the local stress undergone by (C) Al^4, (D) Al^5, and (E) Al^6 atoms under different pressures. The distributions of these different Al species are normalized by the total number of Al atoms.

Next, we analyze the spatial distribution of various bond switching events (decreased, increased, and swapped CN for Al atoms) in a-Al_2O_3. As shown in Fig. 3B, bond switching events in the sample quenched at 0 GPa mainly occur near the fracture surface, with only a few structural arrangements occurring in the bulk glass. Considering the spatial distributions shown in Fig. S6 for the other

samples, we find that the distributions of decreased CN (DC) and swapped CN (SC) are influenced by the applied quenching pressure. Specifically, DC and SC events tend to concentrate near the fracture surface and more DC and SC events occur in the bulk glass with an increase in pressure. This allows for local structural arrangements to dissipate stress during the fracture process. However, the distribution of increased CN (IC) events shows a uniform distribution in the bulk glass despite the change in pressure. Overall, these results suggest densified a-Al_2O_3 facilitates more structural rearrangements to increase its nanoductility.

To describe the formation mechanism of the various types of Al coordination states, we calculate the local stress experienced by the Al atoms in the different samples. As shown in Fig. 3C, we observe that these internal stresses are influenced by the applied pressure during quenching. With an increase in pressure, the stress experienced by Al^4 and Al^5 atoms increases, which is a consequence of their decrease in Voronoi volume under higher pressure. However, for Al^6 atoms, there is no significant pressure-induced shift in the stress distribution. Consistent with the results from Ref. [43], we thus find that the stress on Al increases with CN. This indicates that the maximum stress experienced by each Al atom is related to their CN and, as the pressure increases, Al atoms will gradually increase their CN in order to balance the external pressure during quenching, eventually forcing these Al atoms to remain in their overcoordinated state even after the 0 GPa relaxation. When the system is under plastic deformation, the CN of Al atoms will change in order to balance the external stress. The relationship between CN and stress of Al atoms indicates that Al atoms undergoes DC events, which effectively release the atomic stress. Furthermore, as 7-fold Al atoms are not observed, we deduce that an increase in pressure can increase the fraction of Al^6 without influencing the stress distribution. Although the pressure-induced formation of Al^6 species can increase the extent of decreasing CN events, the most important source of DC events is from Al^5 species. As shown in Fig. S7, the stress on Al^5 atoms in the 0 GPa sample undergoing DC events is in the same range as that of the non-DC events (IC, SC, and unchanged CN). Hence, the bond switching behavior of Al^5 atoms cannot be directly related to the stress analysis.

Atom mobility classification by machine learning

As described above, the bond switching behavior of Al atoms (especially Al^5 atoms) cannot be directly related to intuitive structural descriptors of the nonstrained glass structure, such as coordination numbers, atomic stress, position, *etc*. We therefore adopt the machine learning-based softness metric to investigate whether the mobility of Al atoms and thus their ability to promote plasticity could be encoded in a non-intuitive manner in the spontaneous dynamics of the initial (*i.e.*, unstrained) amorphous structure. We also seek to explore how the mobility of Al atoms is related to the bond switching events under stress. To this end, we first build the SVM hyperplane (Fig. 4A) based on the initial structure of all the a-Al_2O_3 configurations before any load is applied (see Methods section for details). As expected, the classification accuracy greatly depends on the structural input used for training. In detail, when solely relying on radial functions, the classification accuracy can reach 79% (see Fig. S8), with the first peak of the Al-O pair having the largest contribution to the classification as seen from Fig. S9. Notably, we find that this classifier can properly classify the Al atoms as mobile or immobile with an accuracy of 84% and 83% for the training and test datasets, respectively, with the structural input features of radial and angular functions. We also attempted to include the atomic Voronoi volume as an input feature. However,

when trained solely on the Voronoi volume, the classifier yields an accuracy of 56%, which is considerably lower than using the structural functions. We also notice that the accuracy of the classifier does not increase when including both Voronoi volume and structural functions as input, indicating that the latter already includes the knowledge of Voronoi volume (see Fig. S8). We find that the correlation between softness and Voronoi volume is related to the CN of Al atoms. That is, the Voronoi volume decreases with an increase in the CN of the Al atoms. For Al^4 and Al^5 atoms, the Al atoms with larger Voronoi volumes tend to have lower softness (see Fig. S10). This may seem counterintuitive, as larger available free volume should be associated with larger propensity to rearrange and thus higher softness. However, we ascribe this to how the Al^4 and Al^5 atoms with large Voronoi volumes are in metastable equilibrium state of Al^4-to-Al^5 and Al^5-to-Al^6 transitions, respectively, that are prone to rearrange over time. When the amorphous structures are under tension (*e.g.*, $\varepsilon = 0.1$), the softness increases with an increase in the Voronoi volume, but the correlation between softness and Voronoi volume remains the same as in the nonstrained state. This suggests that even though softness is largely dependent on the Voronoi volume, the other structural features are more influential. Moreover, we cannot find a strong correlation between softness and CN (see Fig. S11).

Then, we calculate the softness of each Al atom based on the structural descriptors of Al generated from the configurations at every strain step. This in done in order to investigate the relationship between softness and the fracture process of a-Al_2O_3. We first evaluate how the average softness <*S*> of the system (*i.e.*, averaged over all the Al atoms) evolves during fracture (Fig. 4B). Overall, we find that <*S*> exhibits an increase with the applied strain to a maximum value followed by a drop for all the a-Al_2O_3 samples. Compared with the stress-strain curves in Fig. 1A, we observe that the strain at the maximum <*S*> agrees well with the strain for which stress starts to decrease rapidly, *i.e.*, the onset of crack propagation. Furthermore, we note that the slope of the softness *vs.* strain curve up to the maximum <*S*> varies with the strain value, which can be correlated to the mechanical response. Specifically, as shown in Fig. S12, the slopes are all in the range of 18-26, but can be roughly divided into three different regions depending on the strain. In the first region, the slope is relatively constant or slightly increasing with strain in the elastic region ($\varepsilon < 0.07$). In the second region, the slope rapidly decreases with strain until the structure fully enters the yield region ($0.07 < \varepsilon < 0.09$), which reflects the initiation of plastic regions. At higher strain, the slope increases with some fluctuations, corresponding to the plastic deformation and crack formation in the structure. Based on these results, softness can also capture the early-stage mechanical response under deformation. This indicates that the dynamics of rearrangement at the nanoscale can be captured by the atom-level softness metric (see Fig. S13). We also note that the decrease of <*S*> continues after full fracture, which can be related to the relaxation of the glass, *e.g.*, an increasing amount of IC events, even following fracture (see Fig. 2B).

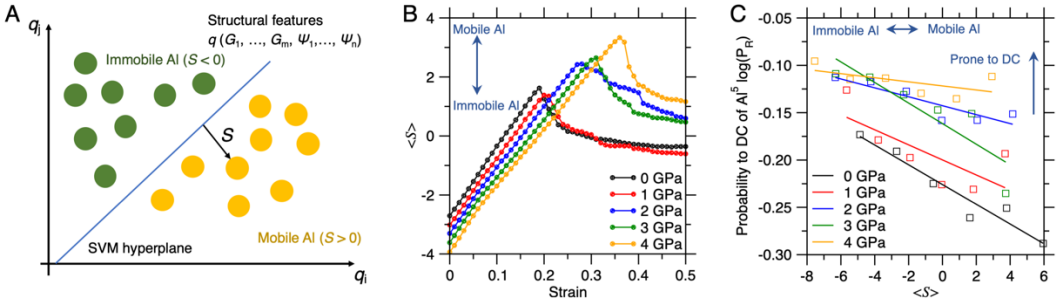

Fig. 4 (A) Illustration of the classifier model used to distinguish mobile Al atoms (in yellow) and immobile Al atoms (in green) through a SVM hyperplane (blue line). The input features are constructed by a combination of radial and angular structure functions (see Eqs. 4 and 5) to describe the local environment of each Al atom. (B) Average softness of Al atoms as a function of the applied strain in the different densified a-Al_2O_3 samples. (C) Probability of Al^5 to decrease its CN during fracture as a function of the average softness $\langle S \rangle$ in the static (non-strained) a-Al_2O_3 samples.

Interestingly, we also observe that the quenching pressure influences the evolution of $\langle S \rangle$ with strain. For the non-strained configurations, $\langle S \rangle$ exhibits a decrease with increasing pressure as the more compact network will give rise to atoms with lower mobility (*i.e.*, lower S). The distribution of S in the non-strained structures also suggest an increasing amount of Al atoms with lower S induced by densification (see Fig. S14A). When strain is applied, $\langle S \rangle$ grows monotonically with strain until the maximum value, indicating that upon tensile deformation, the atoms gradually become "softer" and more prone to reorganization. In contrast, the maximum $\langle S \rangle$ during fracture increases with increasing pressure, indicating that the originally "hard" atoms (*i.e.*, less mobile) can absorb more energy and become activated into "soft" atoms with high mobility. However, when "soft" atoms absorb energy, they are more likely to transform into irreversible defects, *e.g.*, the undercoordinated Al atoms, which exhibit a long tail towards high softness in all the samples upon fracture (see Fig. S14B). We have also observed that the initially "harder" atoms are more likely to transform into "soft" atoms upon deformation (see Fig. S15), indicating that the less mobile atoms are the reservoir of nanoductility. This is consistent with recent work showing that atoms with high self-adaptivity (and thus apparently low softness) under stress can help to suppress crack formation.[44]

Linking atom dynamics to bond switching and fracture

To further establish the relationship between the initial equilibrium, non-strained structure and the long-term far-from-equilibrium fracture response, we combine the concepts of bond switching and softness to explore the link between the dynamics of the atoms and their propensity to undergo bond switching. Based on the results of Fig. 2A, the nanoductility of a-Al_2O_3 is closely related to the events of decreasing CN of Al^5 atoms. As such, we have calculated the probability of Al^5 to decrease its CN (P_R) during the entire fracture process. This calculation is achieved by grouping the Al^5 atoms with similar softness and extracting the fraction of DC events at $\varepsilon = 0.5$. We do so to explore the relationship between P_R and the softness of the non-strained configurations. As shown in Fig. 4C, we find that P_R exhibits an approximate exponential dependence on $\langle S \rangle$, and with a decrease in $\langle S \rangle$, the Al^5 atoms tend to decrease their CN rather than other bond switching behaviors. This correlation is significant as it highlights that the far-from-equilibrium response of the glass upon fracture is largely encoded in its static, unloaded structure. The exponential dependence of P_R on

the softness metric *S* can be reminiscent of an activated procecess as suggested elsewhere,[21] with softness acting as an effective activation energy for Al^5 atoms to decrease their CN. The transformation from "hard" to "soft" atoms occurs continuously upon straining and is accompanied by the energy absorbing bond switching activities. Combined with the results in Fig. S15, we conclude that Al atoms with lower *S* will experience a larger softness increase after fracture, which agrees with the fact that the DC events are the most energy comsuming bond switching activities. This can also be understood from the fact that Al atoms with lower *S* are typically under higher atomic stress, while DC activity can effectively release the atomic stress based on the results shown in Fig. 3C. We also observe an increasing probability of Al^5 to decrease CN in a-Al_2O_3 samples quenched at higher pressure, suggesting that this bond switching event of Al^5 is determined by the softness of the whole system. Based on the results of Ref.[21], the energy barrier of DC activity becomes lower with increasing quenching pressure. Interestingly, as $\langle S \rangle$ of the whole system decreases (for increasing quenching pressure), the dependence of P_R of Al^5 to decrease its CN on individual softness becomes less significant (Fig. 4C).

Since the evolution of average softness can capture the crack propagation, we now investigate the linkage between the distribution of softness and the corresponding fracture states. To this end, we select two systems with widely different degree of nanoductility, namely the samples quenched at 0 and 4 GPa, to investigate the evolution and the spatial distribution of softness during different fracture stages (non-strained state, just prior to fracture, and after fracture, respectively). As shown in Figs. 5A,B, we observe that a-Al_2O_3 quenched at 4 GPa has lower initial softness than the 0 GPa sample. Upon tension, the softness of each atom increases monotonically, and most of the atoms with high softness (red colored spheres) accumulate in a band when the system is about to fracture. The location of the band is found to be related to the origin of fracture, where the atoms exhibit large Voronoi volumes. The band width in a-Al_2O_3 quenched at 4 GPa is larger than that in 0 GPa sample, leading to a more rough fracture surface in a-Al_2O_3 quenched at 4 GPa upon fracture, as also reflected in more surface area created by fracture (see Fig. S16).

For comparison, we also attempt to use Voronoi volume as an indicator of crack propagation. To this end, we track the evolution of softness and Voronoi volume of Al atoms during the loading process. We randomly select the Al atoms with different locations (away from the crack and in the crack) as shown in Fig. S17 and observe that softness features an increasing and then decreasing trend with strain for all the Al atoms (similarly to what is shown in Fig. 4B). However, the Voronoi volume does not systematically follow the same trend, indicating that the increase of softness is not only due to the formation of cavities. We have also investigated the clusters of high volume atoms, observing that the atom with a high atomic volume does not ensure a high softness (see Fig. S18). Although the high-volume atoms also agglomerate upon fracture, the locations of high-softness atoms are more concentrated on the crack initiation region, as also reflected by the formation of more clusters with smaller sizes upon fracture. These results suggest that the softness metric can be used to predict fracture propensity. That is, although the softness metric is trained based on the static structure prior to any applied stress, the spatial distribution of softness can capture the initiation as well as the propagation of a crack during fracture.

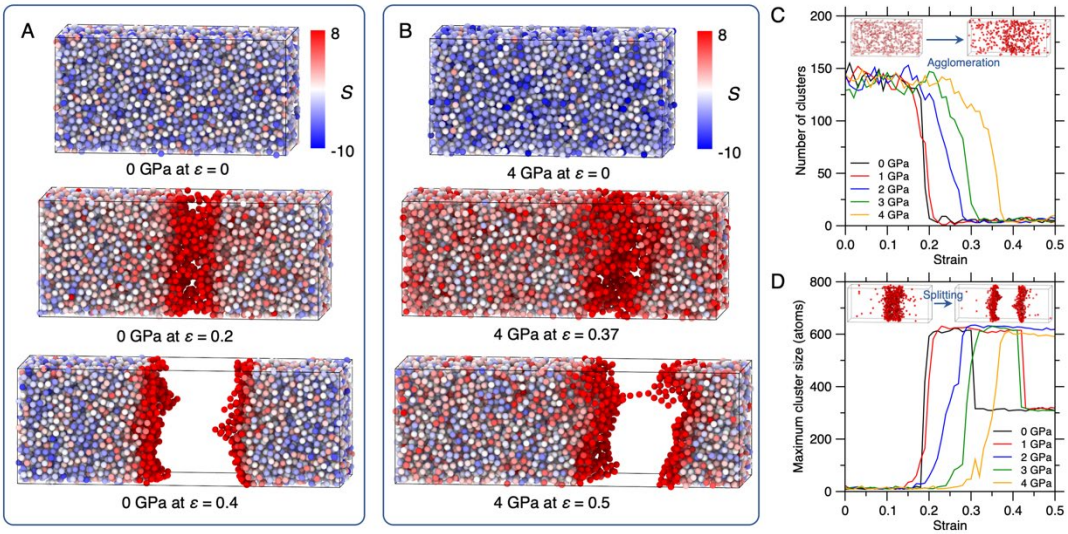

Fig. 5 (A,B) Atomic snapshots of a-Al_2O_3 during the fracture process, where the Al atoms are visualized colored according to their softness. Samples quenched at 0 GPa and 4 GPa are shown in (A) and (B), respectively. (C) The number and (D) maximum size of the high-softness clusters as a function of the applied strain in the different densified a-Al_2O_3 samples. The inset figures in (C) and (D) show the agglomeration and splitting, respectively, of the high-softness Al atoms.

We further investigate the clustering behavior of high-softness Al atoms to understand the relationship between the location of high-softness Al atoms and growth of the crack during fracture. As shown in Fig. 5C, we observe that initially (at low strain) the high-softness atoms are uniformly distributed in the matrix regardless of the densification degree. This is based on the fact that the constant number of 648 high-softness Al atoms are distributed in around 120 clusters. Upon fracture, the number of high-softness clusters significantly decreases. The samples with a more nanoductile fracture response exhibit a decrease in the number of clusters at a relatively higher strain. Fig. 5D shows the maximum size of the high-softness clusters during the fracture process. The strain at which the maximum cluster size starts to increase corresponds to the drop in stress in the stress-strain curves (Fig. 1A) after the crack starts to propagate. The maximum high-softness cluster size for all the systems is about 600 atoms, which is almost equal to the number of high-softness atoms, showing that most of the high-softness atoms agglomerate during fracture. As expected, the end of fracture is also captured by this quantity as a sudden drop of the maximum cluster size, as the cluster is split into two smaller clusters once the sample is fully fractured.

Conclusions

In this work, we have identified the origin of the nanoductility in densified a-Al_2O_3 samples by establishing the correlation between the initial static structure and dynamics captured by the so-called "softness" metric, local bond switching events, and the long-term fracture behavior. We find that the origin of nanoductility can be attributed to the increased amount of Al^5 and Al^6 atoms in the densified samples that have high propensity to decrease their coordination number during fracture. Based on classification-based machine learning calculations, we reveal that the long-time dynamics of the atoms upon fracture are hidden in the initial static structure of a-Al_2O_3, before any load is applied. Although the machine learning model is trained based on the spontaneous dynamics, it properly captures the far-from-equilibrium dynamics upon loading. This approach thus allows us to predict the propensity for crack propagation in a realistic amorphous oxide based solely on the

machine-learned softness metric. In the present case, we show that almost all the Al^6 and Al^5 atoms with lower softness atoms tend to decrease their coordination number during fracture. Our results also suggest that the formation of high-mobility regions leads to the failure of the system. Based on these observations, we envision that machine learning can help to decode the hidden correlations between nanoscale structural features and mechanical properties in disordered materials, and consequently help to design tougher oxide glasses by rational design of the atomic structure.

Methods

Sample preparation

In this study, we adopted the Large-scale Atomic/Molecular Massively Parallel Simulator (LAMMPS) software[45] to perform MD simulations of a-Al_2O_3 with the classical potential of Matsui,[46] which has been widely used in reproducing the structure and mechanical properties of various phases of Al_2O_3.[37,47–49] The long range Coulombic interaction was calculated using the Particle-Particle-Mech (PPPM) summation with an accuracy of 10^{-5}.[50] The motion of atoms was described by the velocity-Verlet integration algorithm with a time step of 1 fs. A Nosé-Hoover thermostat and barostat were applied to control the temperature and pressure, respectively, when applicable. Periodic boundary conditions were applied in all directions.

We generated the a-Al_2O_3 configurations through the process introduced by Gutiérrez *et al.*[49] Specifically, 1620 Al_2O_3 units (8100 atoms) were placed in an orthorhombic box at a density of 2.75 g/cm^3. Then the systems were melted in the *NVT* ensemble at 5000 K for 45 ps to ensure the loss of any memory of the initial structure. Afterwards the structure was cooled to 3000 K in 10 ps, and further equilibrated at 3000 K for 45 ps. The density of the system was changed to 3.175 g/cm^3, and equilibrated for an additional 45 ps in the *NVT* ensemble. The next step was to cool the system down to 300 K in the *NPT* ensemble under different pressures (0, 1, 2, 3, and 4 GPa, respectively) over 650 ps. The systems were then successively relaxed in the *NVT* and *NPT* ensembles at 300 K and 0 pressure for another 35 ps. This process of cooling from high temperature also ensures that the samples quenched from different pressures are independent of each other, since the high temperature melting removes any memory of the initial structure. The utilized cooling and relaxation processes were adopted from Ref.[37] and found to be long enough to reproduce the material properties of a-Al_2O_3. The structure of a-Al_2O_3 quenched at 0 GPa after relaxation is shown in Fig. S19A. Although the glasses were eventually relaxed at zero pressure, the densification during quenching was permanent since the system remains frozen in its densified state once it reaches the glassy state. As shown in Fig. S19B, the applied pressure can effectively densify the a-Al_2O_3 structure, with a linear increase in density with pressure.

Fracture simulations

The deformation and fracture behavior of a-Al_2O_3 was analyzed by applying a uniaxial tensile deformation. We note that the fracture behavior of a-Al_2O_3 strongly depends on the loading conditions as mentioned in Ref.[37]. Here, we applied two tensile protocols to systematically investigate the effect of loading mode on fracture. Before the tensile simulations, the orthorhombic a-Al_2O_3 configurations were duplicated in the *x*-direction so that the loading was applied to the longer direction. The resulting structures (consisting of 16,200 atoms) were equilibrated at 300 K and zero pressure in the *NPT* ensemble for 100 ps before deformation.

The first loading condition was adopted from Ref. [37]. Specifically, a constant strain rate of 5×10^{10} s^{-1} was applied along the *x*-direction, while the barostat was used to keep the lateral directions at zero stress (*i.e.*, "plane stress" conditions). During the tensile simulation, the system was maintained at 300 K. The duration of the tensile simulation was 1 ns, leading to a total strain of 50%. The stress-strain curve was constructed based on the stress component in the *x*-direction and corresponding strain.

The second loading condition was adopted from Ref. [42]. In this loading mode, the system along the *x*-direction was deformed by small strain steps of 1%, while the sizes in lateral directions were fixed (*i.e.*, "plane strain" conditions). At each step of deformation, the structure was subjected to an initial energy minimization and then equilibrated in the *NVT* ensemble at 300 K for 10 ps before sampling the stress. This procedure was iteratively repeated until the structure was fully fractured.

Cumulative non-affine displacement *D*

The cumulative non-affine displacement *D* of each Al atom upon loading was computed to investigate the irreversible structural rearrangements, which were responsible for the plasticity during the fracture process. *D* has previously been successfully applied in capturing the number and magnitude of the local plastic events occurring in the atomic structure during fracture processes.[42] This concept originates from the non-affine square displacement D^2_{min}, which has been widely used in identifying the activation of STZs upon deformation.[24,51] The quantity D^2_{min} describes the degree of local reorganization of atoms by subtracting the displacement induced by the affine deformation of the simulation box. The degree of local reorganization of each atom in the strained configuration can be quantitatively measured by comparing with the non-strained configuration. However, since the configuration will experience significant changes once fractured, we instead used a cumulative non-affine displacement *D*, which accounts for the entire fracture process by properly considering the local ductile events.[42] This quantity is calculated by summing up the non-affine displacements at each small strain step *s*:

$$D = \sum_{s=1}^{n} \sqrt{\Delta D^2_{s,min}} \qquad (1)$$

where $\Delta D^2_{s,min}$ is the incremental non-affine square displacement with each increment of strain *s* and *n* is the total number of strain steps. The cut-off used for the calculation of $D^2_{s,min}$ was set to 4 Å, which covers the 1st and 2nd coordination shells of Al atoms.

Local atomic stresses

We calculated the local stress experienced by each Al atom by adopting the formalism of "stress per atom".[52] Note that, strictly speaking, stress is ill-defined for individual atoms and can only be meaningful when calculated for an ensemble of atoms. To overcome these difficulties, we here adopt the concept of "stress per atom" introduced by Egami,[53] wherein the local atomic local stress tensor $\sigma_i^{\alpha\beta}$ is defined by expressing the contribution of each atom *i* to the viral of the system,

$$\sigma_i^{\alpha\beta} V_i = \sum_j r_{ij}^{\alpha} \cdot F_{ij}^{\beta} \qquad (2)$$

where V_i is the volume of atom *i*, r_{ij} and F_{ij} are the distance and interatomic force, respectively, of

atom *j* applied to atom *i,* and the indices α and β represent the projections of these vectors along the *x*, *y*, and *z* directions. The volume V_i of each atom was calculated based on the Voronoi tessellation. The local hydrostatic stress undergone by each atom can be calculated by the trace of the stress tensor. By convention, a positive stress denotes a state of local tension, while a negative one refers to a state of compression. The presence of local atomic stress does not imply that the system is under any macroscopic stress, namely, some atoms are locally under compression whereas others are locally under tension and eventually mutually compensate each other so that the whole system can still remain under zero pressure. This formalism has previously been successfully adopted to amorphous materials.[43,44]

Coordination number and bond switching analyses

During the fracture process, plasticity is associated with the atomic arrangements that occur due to bond breaking and reformation. We have thus analyzed the changes in coordination number (CN) and bond switching activities as a function of the applied tensile strain. To analyze the CNs, we first calculated the partial pair distribution functions. The cut-off between Al and O were selected to be the distance at the minima after the first peak in the pair distribution function. To this end, partial pair distribution functions of Al-O and Al-Al are shown in Fig. S20. The atoms of Al and O are considered bonded if they are within the cut-off. The cut-off selected in this study was 2.25 Å for Al-O pairs, and the CN of Al was defined as the number O atoms within this cut-off.

The bond switching analysis was carried out by comparing the CN and the identity of the neighboring atom of each individual atom with its initial non-strained structure. If the CN has decreased or increased, then the atoms were labelled as DC or IC, respectively. If both the CN and the neighboring atoms remain unchanged, then the atoms were labelled as UC. Otherwise, the atoms were counted as SC, indicating the unchanged CN with at least one different neighboring atom. A schematic illustration of these different bond switching events is shown in Fig. S21. Note that the time intervals (2 ps) or strain step (0.01) of adjacent frames to calculate bond switching was found to be large enough to allow for bond rotation and reconnection.[31,37]

Machine learning classification

Following the procedure in Ref. [22] to build the input features of the SVM model, we first analyzed the local static, unstrained structure of the system. The output of the SVM model is determined from the spontaneous rearrangements of the Al atoms under 300 K (in unstrained conditions). As such, the training dataset used to train the SVM model is solely based on the thermal vibrations of non-strained structures at 300 K.

In detail, the initially non-strained configurations were equilibrated in the *NVT* ensemble at 300 K for 200 ps, while the trajectory was recorded for rearrangement analysis. In order to build up the SVM model without any prior knowledge of deformation, the rearrangements of each Al atom were calculated by the p_{hop} metric proposed by Candelier *et al.*,[56] which has been used extensively to identify rearrangements in amorphous materials.[22,57] To calculate p_{hop}, we used a timescale $t_R = 6$ ps, which was found to be commensurate with the time required for rearrangements. For an atom at a given time frame *t*, two time intervals A and B are defined as $[t - t_{R/2}, t]$ and $[t, t + t_{R/2}]$, respectively. Then p_{hop} of atom *i* at time *t* can be calculated as follows:

$$p_{\mathrm{hop}}(t) = \sqrt{\langle (r_i - \langle r_i \rangle_{\mathrm{B}})^2 \rangle_{\mathrm{A}} \langle (r_i - \langle r_i \rangle_{\mathrm{A}})^2 \rangle_{\mathrm{B}}} \qquad (3)$$

where $\langle\rangle_{\mathrm{A}}$ and $\langle\rangle_{\mathrm{B}}$ are averages over the time intervals A and B, respectively. When an atom is caged, $\langle r_i \rangle_{\mathrm{A}}$ will approximately be equal to $\langle r_i \rangle_{\mathrm{B}}$, which will result in a p_{hop} value comparable to the scale of fluctuations within its cage. When p_{hop} exceeds a threshold value and exhibits a peak at a duration of time t, it represents that the particle has undergone a rearrangement. Here, we took the threshold value to be 0.2 Å^2, which was found to be large enough for identifying the rearrangement of the Al atoms (see Fig. S22A). We find the same trend as in Ref. [22], *i.e.*, the accuracy of identifying mobile atoms will saturate when the threshold value is large enough. For example, when increasing the threshold to 0.5 Å^2, the accuracy can reach 0.85, but then the number of rearrangement events has decreased to around 700, which will negatively influence the generalization ability of the SVM model. After applying the threshold value of 0.2 Å^2 to all the investigated a-Al_2O_3 samples, we accumulated almost 8000 rearrangement events. Since most of the inert atoms have a p_{hop} value below 0.05 (see Fig. S22B), as also mentioned in Ref. [22], the non-rearrangement events are defined as those with $p_{\mathrm{hop}} < 0.05$. Meanwhile, we also randomly selected the same number (8000) of events without rearrangements.

The inputs in the SVM models are the descriptors of local structures of selected atoms. As described in Ref. [19], we used the same radial and angular structure functions to describe the local structure.

$$G(k;\mu) = \sum_i e^{-(r_{ik}-\mu)^2/L^2} \qquad (4)$$

$$\Psi(k;\xi,\lambda,\zeta) = \sum_{i,j} \mathrm{e}^{-(r_{ik}^2+r_{jk}^2+r_{ij}^2)/\xi^2} \left(1 + \lambda \cos\theta_{ijk}\right)^{\zeta} \qquad (5)$$

Here, r_{ik} is the distance between atoms i and k and the range of μ values is selected to be between 0.6 and 10 Å, with an increment of 0.2 Å. The classification accuracy for different series of μ values is presented in Fig. S23, showing that although the first peak of the Al-O radial function has the largest contribution, the long-range structure also influences the mobility of the atoms. The window parameter L was set to be 0.2 Å. θ_{ijk} is the angle between atoms i, j, and k. For the parameters ξ, λ, and ζ in the angular structure functions, we used a series of combinations to characterize different aspects of an atom's angular environment (see the values in Ref. [19]).

Based on the structural descriptors and the corresponding labels (rearranging or non-rearranging), we then adopted the linear SVM algorithm by using the LIBSVM package[58] to train a classifier, which can be used to distinguish the rearranging and non-rearranging atoms based on their subsequent local environment. Consistent with the results of Ref. [19], we found the accuracy of the classifier to be insensitive to the regularization C parameter of SVM when $C > 0.1$. The cross-validation was carried out on random train/test splits while ensuring the independency of the training and test sets by avoiding the use of the same atoms in both the training and test processes. We also attempted to split the original dataset based on time series, *i.e.*, 0-160 ps for training and 160-200 ps for testing, and this yielded a similar accuracy result as that from the applied random splitting. After cross-validation, we used a C parameter of 1, which yielded accuracies of both the training and test sets of around 83%. The softness S_{i} of atom i is defined as the orthogonal distance between its position in the feature space and the SVM decision boundary hyperplane (see Fig. 4A).

Finally, we also tested the generalization of the SVM model when trained on a partial dataset. As shown in Table S1, we found that the generalization does not significantly decrease when using partial dataset for training and the rest for testing (decrease from 0.833 to 0.798). The worst case yields an accuracy of only 0.693 when using the 0 GPa data as training set and 4 GPa data as test set. This highlights the importance of including all the datasets to get the best prediction.

High-mobility cluster analysis

Here, the Al atoms with high mobility were defined as Al atoms with the top 10% highest softness, which was defined dynamically at each strain step. We used the OVITO software[59] to visualize and perform a cluster analysis of a-Al_2O_3 configurations during tension. To this end, high-softness clusters were defined as a group of *n* Al atoms with high-softness connected by O atoms, *i.e.*, when two Al atoms within a specified cut-off were considered to be connected. As shown above, the cluster analysis focused solely on the Al atoms. A cluster is defined as a group of *n* Al atoms within a cut-off of 3.7 Å, which is the minimum after the first peak in the Al-Al partial pair distribution function (see Fig. S20B).

Supporting Information

The Supporting Information is available free of charge on the ACS Publications website at DOI:XXX. Additional data including the mechanical and structural properties of a-Al_2O_3; the evolution and distribution of bond switching activities; tuning of hyper parameters for the machine learning model; machine learning model performance with different features; correlations between softness and structural properties; and correlations between softness and dynamic properties.

Author Contributions

M.M.S conceived the study. T.D., M.M.S., and M.B. planned the computational work. T.D. performed the molecular dynamics simulations, structural analyses, and machine learning calculations, with assistance from H.L., L.T., and S.S.S. T.D. and M.M.S. wrote the manuscript, with revisions from M.B., L.T., S.S.S., and H.L. All authors participated in discussing the results.

Conflicts of interest

The authors declare no competing financial interests.

Acknowledgements

This work was supported by VILLUM FONDEN (grant no. 13253). We also thank Aalborg University for access to computational resources through CLAAUDIA. T.D. is supported by a Marie Skłodowska-Curie Individual Fellowship (101018156). M.B. acknowledges the support from the National Science Foundation under grants DMREF-1922167, CMMI-1762292, and CAREER-1944510.

References

(1) Lawn, B. R.; Swain, M. V. Microfracture Beneath Point Indentations in Brittle Solids. *J. Mater. Sci.* **1975**, *10* (1), 113–122. https://doi.org/10.1007/BF00541038.
(2) Griffith, A. A.; Taylor, G. I. VI. The Phenomena of Rupture and Flow in Solids. *Phil. Trans. Royal Soc. London. Ser. A* **1921**, *221* (582–593), 163–198.

https://doi.org/10.1098/rsta.1921.0006.
(3) Yoshida, S. Indentation Deformation and Cracking in Oxide Glass –Toward Understanding of Crack Nucleation. *J. Non-Cryst. Solids: X* **2019**, *1*, 100009. https://doi.org/10.1016/j.nocx.2019.100009.
(4) Wondraczek, L.; Mauro, J. C.; Eckert, J.; Kühn, U.; Horbach, J.; Deubener, J.; Rouxel, T. Towards Ultrastrong Glasses. *Adv. Mater.* **2011**, *23* (39), 4578–4586. https://doi.org/10.1002/adma.201102795.
(5) Pineau, A.; Benzerga, A. A.; Pardoen, T. Failure of Metals I: Brittle and Ductile Fracture. *Acta Mater.* **2016**, *107*, 424–483. https://doi.org/10.1016/j.actamat.2015.12.034.
(6) Xi, X. K.; Zhao, D. Q.; Pan, M. X.; Wang, W. H.; Wu, Y.; Lewandowski, J. J. Fracture of Brittle Metallic Glasses: Brittleness or Plasticity. *Phys. Rev. Lett.* **2005**, *94* (12), 125510. https://doi.org/10.1103/PhysRevLett.94.125510.
(7) Schroers, J.; Johnson, W. L. Ductile Bulk Metallic Glass. *Phys. Rev. Lett.* **2004**, *93* (25), 255506. https://doi.org/10.1103/PhysRevLett.93.255506.
(8) Ketkaew, J.; Chen, W.; Wang, H.; Datye, A.; Fan, M.; Pereira, G.; Schwarz, U. D.; Liu, Z.; Yamada, R.; Dmowski, W.; Shattuck, M. D.; O'Hern, C. S.; Egami, T.; Bouchbinder, E.; Schroers, J. Mechanical Glass Transition Revealed by the Fracture Toughness of Metallic Glasses. *Nat. Commun.* **2018**, *9* (1), 3271. https://doi.org/10.1038/s41467-018-05682-8.
(9) Li, W.; Gao, Y.; Bei, H. On the Correlation between Microscopic Structural Heterogeneity and Embrittlement Behavior in Metallic Glasses. *Sci. Rep.* **2015**, *5* (1), 14786. https://doi.org/10.1038/srep14786.
(10) Yuan, F.; Huang, L. Brittle to Ductile Transition in Densified Silica Glass. *Sci. Rep.* **2014**, *4* (1), 5035. https://doi.org/10.1038/srep05035.
(11) Greer, A. L.; Cheng, Y. Q.; Ma, E. Shear Bands in Metallic Glasses. *Mater. Sci. Eng.: R: Rep.* **2013**, *74* (4), 71–132. https://doi.org/10.1016/j.mser.2013.04.001.
(12) Cheng, Y. Q.; Ma, E. Atomic-Level Structure and Structure–Property Relationship in Metallic Glasses. *Prog. Mater. Sci.* **2011**, *56* (4), 379–473. https://doi.org/10.1016/j.pmatsci.2010.12.002.
(13) Nicolas, A.; Ferrero, E. E.; Martens, K.; Barrat, J.-L. Deformation and Flow of Amorphous Solids: Insights from Elastoplastic Models. *Rev. Mod. Phys.* **2018**, *90* (4), 045006. https://doi.org/10.1103/RevModPhys.90.045006.
(14) Sollich, P.; Lequeux, F.; Hébraud, P.; Cates, M. E. Rheology of Soft Glassy Materials. *Phys. Rev. Lett.* **1997**, *78* (10), 2020–2023. https://doi.org/10.1103/PhysRevLett.78.2020.
(15) Argon, A. S. Plastic Deformation in Metallic Glasses. *Acta Metall.* **1979**, *27* (1), 47–58. https://doi.org/10.1016/0001-6160(79)90055-5.
(16) Falk, M. L.; Langer, J. S. Dynamics of Viscoplastic Deformation in Amorphous Solids. *Phys. Rev. E* **1998**, *57* (6), 7192–7205. https://doi.org/10.1103/PhysRevE.57.7192.
(17) Ding, J.; Patinet, S.; Falk, M. L.; Cheng, Y.; Ma, E. Soft Spots and Their Structural Signature in a Metallic Glass. *Proc. Natl. Acad. Sci. U. S. A.* **2014**, *111* (39), 14052–14056. https://doi.org/10.1073/pnas.1412095111.

(18) Richard, D.; Ozawa, M.; Patinet, S.; Stanifer, E.; Shang, B.; Ridout, S. A.; Xu, B.; Zhang, G.; Morse, P. K.; Barrat, J.-L.; Berthier, L.; Falk, M. L.; Guan, P.; Liu, A. J.; Martens, K.; Sastry, S.; Vandembroucq, D.; Lerner, E.; Manning, M. L. Predicting Plasticity in Disordered Solids from Structural Indicators. *Phys. Rev. Mater.* **2020**, *4* (11), 113609. https://doi.org/10.1103/PhysRevMaterials.4.113609.
(19) Cubuk, E. D.; Schoenholz, S. S.; Rieser, J. M.; Malone, B. D.; Rottler, J.; Durian, D. J.; Kaxiras, E.; Liu, A. J. Identifying Structural Flow Defects in Disordered Solids Using Machine-Learning Methods. *Phys. Rev. Lett.* **2015**, *114* (10), 108001. https://doi.org/10.1103/PhysRevLett.114.108001.
(20) Fan, Z.; Ma, E. Predicting Orientation-Dependent Plastic Susceptibility from Static Structure in Amorphous Solids *via* Deep Learning. *Nat. Commun.* **2021**, *12* (1), 1506. https://doi.org/10.1038/s41467-021-21806-z.
(21) Liu, H.; Xiao, S.; Tang, L.; Bao, E.; Li, E.; Yang, C.; Zhao, Z.; Sant, G.; Smedskjaer, M. M.; Guo, L.; Bauchy, M. Predicting the Early-Stage Creep Dynamics of Gels from Their Static Structure by Machine Learning. *Acta Mater.* **2021**, *210*, 116817. https://doi.org/10.1016/j.actamat.2021.116817.
(22) Schoenholz, S. S.; Cubuk, E. D.; Sussman, D. M.; Kaxiras, E.; Liu, A. J. A Structural Approach to Relaxation in Glassy Liquids. *Nat. Phys.* **2016**, *12* (5), 469–471. https://doi.org/10.1038/nphys3644.
(23) Bapst, V.; Keck, T.; Grabska-Barwińska, A.; Donner, C.; Cubuk, E. D.; Schoenholz, S. S.; Obika, A.; Nelson, A. W. R.; Back, T.; Hassabis, D.; Kohli, P. Unveiling the Predictive Power of Static Structure in Glassy Systems. *Nat. Phys.* **2020**, *16* (4), 448–454. https://doi.org/10.1038/s41567-020-0842-8.
(24) Cubuk, E. D.; Ivancic, R. J. S.; Schoenholz, S. S.; Strickland, D. J.; Basu, A.; Davidson, Z. S.; Fontaine, J.; Hor, J. L.; Huang, Y.-R.; Jiang, Y.; Keim, N. C.; Koshigan, K. D.; Lefever, J. A.; Liu, T.; Ma, X.-G.; Magagnosc, D. J.; Morrow, E.; Ortiz, C. P.; Rieser, J. M.; Shavit, A.; *et al.* Structure-Property Relationships from Universal Signatures of Plasticity in Disordered Solids. *Science* **2017**, *358* (6366), 1033–1037. https://doi.org/10.1126/science.aai8830.
(25) Sharp, T. A.; Thomas, S. L.; Cubuk, E. D.; Schoenholz, S. S.; Srolovitz, D. J.; Liu, A. J. Machine Learning Determination of Atomic Dynamics at Grain Boundaries. *Proc. Natl. Acad. Sci. U. S. A.* **2018**, *115* (43), 10943–10947. https://doi.org/10.1073/pnas.1807176115.
(26) Sussman, D. M.; Schoenholz, S. S.; Cubuk, E. D.; Liu, A. J. Disconnecting Structure and Dynamics in Glassy Thin Films. *Proc. Natl. Acad. Sci. U. S. A.* **2017**, *114* (40), 10601–10605. https://doi.org/10.1073/pnas.1703927114.
(27) Freitas, R.; Reed, E. J. Uncovering the Effects of Interface-Induced Ordering of Liquid on Crystal Growth Using Machine Learning. *Nat. Commun.* **2020**, *11* (1), 3260. https://doi.org/10.1038/s41467-020-16892-4.
(28) de Pablo, J. J.; Jackson, N. E.; Webb, M. A.; Chen, L.-Q.; Moore, J. E.; Morgan, D.; Jacobs, R.; Pollock, T.; Schlom, D. G.; Toberer, E. S.; Analytis, J.; Dabo, I.; DeLongchamp, D. M.; Fiete, G. A.; Grason, G. M.; Hautier, G.; Mo, Y.; Rajan, K.; Reed, E. J.; Rodriguez, E.; *et al.* New Frontiers for the Materials Genome Initiative. *npj Comput. Mater.* **2019**, *5* (1), 1–23. https://doi.org/10.1038/s41524-019-0173-4.

(29) van der Scheer, P.; van de Laar, T.; van der Gucht, J.; Vlassopoulos, D.; Sprakel, J. Fragility and Strength in Nanoparticle Glasses. *ACS Nano* **2017**, *11* (7), 6755–6763. https://doi.org/10.1021/acsnano.7b01359.
(30) Chatterjee, D.; Annamareddy, A.; Ketkaew, J.; Schroers, J.; Morgan, D.; Voyles, P. M. Fast Surface Dynamics on a Metallic Glass Nanowire. *ACS Nano* **2021**, *15* (7), 11309–11316. https://doi.org/10.1021/acsnano.1c00500.
(31) Luo, J.; Wang, J.; Bitzek, E.; Huang, J. Y.; Zheng, H.; Tong, L.; Yang, Q.; Li, J.; Mao, S. X. Size-Dependent Brittle-to-Ductile Transition in Silica Glass Nanofibers. *Nano Lett.* **2016**, *16* (1), 105–113. https://doi.org/10.1021/acs.nanolett.5b03070.
(32) Zhang, Y.; Huang, L.; Shi, Y. Silica Glass Toughened by Consolidation of Glassy Nanoparticles. *Nano Lett.* **2019**, *19* (8), 5222–5228. https://doi.org/10.1021/acs.nanolett.9b01634.
(33) Zheng, K.; Wang, C.; Cheng, Y.-Q.; Yue, Y.; Han, X.; Zhang, Z.; Shan, Z.; Mao, S. X.; Ye, M.; Yin, Y.; Ma, E. Electron-Beam-Assisted Superplastic Shaping of Nanoscale Amorphous Silica. *Nat. Commun.* **2010**, *1* (1), 24. https://doi.org/10.1038/ncomms1021.
(34) Yang, Y.; Kushima, A.; Han, W.; Xin, H.; Li, J. Liquid-Like, Self-Healing Aluminum Oxide during Deformation at Room Temperature. *Nano Lett.* **2018**. https://doi.org/10.1021/acs.nanolett.8b00068.
(35) García Ferré, F.; Bertarelli, E.; Chiodoni, A.; Carnelli, D.; Gastaldi, D.; Vena, P.; Beghi, M. G.; Di Fonzo, F. The Mechanical Properties of a Nanocrystalline Al2O3/a-Al2O3 Composite Coating Measured by Nanoindentation and Brillouin Spectroscopy. *Acta Mater.* **2013**, *61* (7), 2662–2670. https://doi.org/10.1016/j.actamat.2013.01.050.
(36) Calvié, E.; Joly-Pottuz, L.; Esnouf, C.; Clément, P.; Garnier, V.; Chevalier, J.; Jorand, Y.; Malchère, A.; Epicier, T.; Masenelli-Varlot, K. Real Time TEM Observation of Alumina Ceramic Nano-Particles during Compression. *J. Eur. Ceram. Soc.* **2012**, *32* (10), 2067–2071. https://doi.org/10.1016/j.jeurceramsoc.2012.02.029.
(37) Frankberg, E. J.; Kalikka, J.; Ferré, F. G.; Joly-Pottuz, L.; Salminen, T.; Hintikka, J.; Hokka, M.; Koneti, S.; Douillard, T.; Saint, B. L.; Kreiml, P.; Cordill, M. J.; Epicier, T.; Stauffer, D.; Vanazzi, M.; Roiban, L.; Akola, J.; Fonzo, F. D.; Levänen, E.; Masenelli-Varlot, K. Highly Ductile Amorphous Oxide at Room Temperature and High Strain Rate. *Science* **2019**, *366* (6467), 864–869. https://doi.org/10.1126/science.aav1254.
(38) van der Rest, A.; Idrissi, H.; Henry, F.; Favache, A.; Schryvers, D.; Proost, J.; Raskin, J.-P.; Van Overmeere, Q.; Pardoen, T. Mechanical Behavior of Ultrathin Sputter Deposited Porous Amorphous Al_2O_3 Films. *Acta Mater.* **2017**, *125*, 27–37. https://doi.org/10.1016/j.actamat.2016.11.037.
(39) Mercier, D.; Mandrillon, V.; Parry, G.; Verdier, M.; Estevez, R.; Bréchet, Y.; Maindron, T. Investigation of the Fracture of Very Thin Amorphous Alumina Film during Spherical Nanoindentation. *Thin Solid Films* **2017**, *638*, 34–47. https://doi.org/10.1016/j.tsf.2017.07.040.
(40) Jen, S.-H.; Bertrand, J. A.; George, S. M. Critical Tensile and Compressive

Strains for Cracking of Al_2O_3 Films Grown by Atomic Layer Deposition. *J. Appl. Phys.* **2011**, *109* (8), 084305. https://doi.org/10.1063/1.3567912.
(41) To, T.; Sørensen, S. S.; Christensen, J. F. S.; Christensen, R.; Jensen, L. R.; Bockowski, M.; Bauchy, M.; Smedskjaer, M. M. Bond Switching in Densified Oxide Glass Enables Record-High Fracture Toughness. *ACS Appl. Mater. Interfaces* **2021**, *13* (15), 17753–17765. https://doi.org/10.1021/acsami.1c00435.
(42) Tang, L.; Liu, H.; Ma, G.; Du, T.; Mousseau, N.; Zhou, W.; Bauchy, M. The Energy Landscape Governs Ductility in Disordered Materials. *Mater. Horiz.* **2021**, 10.1039.D0MH00980F. https://doi.org/10.1039/D0MH00980F.
(43) Zhao, C.; Zhou, W.; Zhou, Q.; Zhang, Y.; Liu, H.; Sant, G.; Liu, X.; Guo, L.; Bauchy, M. Precipitation of Calcium–Alumino–Silicate–Hydrate Gels: The Role of the Internal Stress. *J. Chem. Phys.* **2020**, *153* (1), 014501. https://doi.org/10.1063/5.0010476.
(44) Januchta, K.; Youngman, R. E.; Goel, A.; Bauchy, M.; Logunov, S. L.; Rzoska, S. J.; Bockowski, M.; Jensen, L. R.; Smedskjaer, M. M. Discovery of Ultra-Crack-Resistant Oxide Glasses with Adaptive Networks. *Chem. Mater.* **2017**, *29* (14), 5865–5876. https://doi.org/10.1021/acs.chemmater.7b00921.
(45) Plimpton, S. Fast Parallel Algorithms for Short-Range Molecular Dynamics. *J. Comput. Phys.* **1995**, *117* (1), 1–19. https://doi.org/10.1006/jcph.1995.1039.
(46) Matsui, M. A Transferable Interatomic Potential Model for Crystals and Melts in the System CaO-MgO-Al_2O_3-SiO_2. *Mineral. Mag.* **1994**, *58A*, 571-572. https://doi.org/10.1180/MINMAG.1994.58A.2.34.
(47) Ahuja, R.; Belonoshko, A. B.; Johansson, B. Melting and Liquid Structure of Aluminum Oxide Using a Molecular-Dynamics Simulation. *Phys. Rev. E* **1998**, *57* (2), 1673–1676. https://doi.org/10.1103/PhysRevE.57.1673.
(48) Gutiérrez, G.; Belonoshko, A. B.; Ahuja, R.; Johansson, B. Structural Properties of Liquid Al_2O_3: A Molecular Dynamics Study. *Phys. Rev. E* **2000**, *61* (3), 2723–2729. https://doi.org/10.1103/PhysRevE.61.2723.
(49) Gutiérrez, G.; Johansson, B. Molecular Dynamics Study of Structural Properties of Amorphous Al_2O_3. *Phys. Rev. B* **2002**, *65* (10), 104202. https://doi.org/10.1103/PhysRevB.65.104202.
(50) Hockney, R. W.; Eastwood, J. W. *Computer Simulation Using Particles*; Taylor and Francis: New York, 1988.
(51) Maloney, C. E.; Lemaître, A. Amorphous Systems in Athermal, Quasistatic Shear. *Phys. Rev. E* **2006**, *74* (1), 016118. https://doi.org/10.1103/PhysRevE.74.016118.
(52) Thompson, A. P.; Plimpton, S. J.; Mattson, W. General Formulation of Pressure and Stress Tensor for Arbitrary Many-Body Interaction Potentials under Periodic Boundary Conditions. *J. Chem. Phys.* **2009**, *131* (15), 154107. https://doi.org/10.1063/1.3245303.
(53) Egami, T. Atomic Level Stresses. *Prog. Mater. Sci.* **2011**, *56* (6), 637–653. https://doi.org/10.1016/j.pmatsci.2011.01.004.
(54) Zhou, Q.; Wang, M.; Guo, L.; Boolchand, P.; Bauchy, M. Intermediate Phase in Calcium–Silicate–Hydrates: Mechanical, Structural, Rigidity, and Stress

Signatures. *Front. Mater.* **2019**, *6*. https://doi.org/10.3389/fmats.2019.00157.
(55) Du, T.; Li, H.; Sant, G.; Bauchy, M. New Insights into the Sol–Gel Condensation of Silica by Reactive Molecular Dynamics Simulations. *J. Chem. Phys.* **2018**, *148* (23), 234504. https://doi.org/10.1063/1.5027583.
(56) Candelier, R.; Widmer-Cooper, A.; Kummerfeld, J. K.; Dauchot, O.; Biroli, G.; Harrowell, P.; Reichman, D. R. Spatiotemporal Hierarchy of Relaxation Events, Dynamical Heterogeneities, and Structural Reorganization in a Supercooled Liquid. *Phys. Rev. Lett.* **2010**, *105* (13), 135702. https://doi.org/10.1103/PhysRevLett.105.135702.
(57) Smessaert, A.; Rottler, J. Distribution of Local Relaxation Events in an Aging Three-Dimensional Glass: Spatiotemporal Correlation and Dynamical Heterogeneity. *Phys. Rev. E* **2013**, *88* (2), 022314. https://doi.org/10.1103/PhysRevE.88.022314.
(58) Chang, C.-C.; Lin, C.-J. LIBSVM: A Library for Support Vector Machines. *ACM Trans. Intell. Syst. Technol.* **2011**, *2* (3), 27:1-27:27. https://doi.org/10.1145/1961189.1961199.
(59) Stukowski, A. Visualization and Analysis of Atomistic Simulation Data with OVITO–The Open Visualization Tool. *Modelling Simul. Mater. Sci. Eng.* **2009**, *18* (1), 015012. https://doi.org/10.1088/0965-0393/18/1/015012.